ADVANCED MATERIALS
www.advmat.de

Semicrystalline Conjugated Polymers with Well-Defined Active Sites for Nitrogen Fixation in a Seawater Electrolyte

Feili Lai, Jiajia Huang, Xunfan Liao,* Wei Zong, Lingfeng Ge, Feng Gan, Yuting Fang, Yue-E Miao, Johan Hofkens,* Tianxi Liu,* and Liming Dai**

Faradaic efficiency for the nitrogen reduction reaction (NRR) is often limited by low N_2 solubility in the electrolyte, while a large number of intimate contacts between the electrolyte and solid catalyst can also inevitably sacrifice many active sites for the NRR. Here, it is reported that a "quasi-gas–solid" interface formed in donor–acceptor-based conjugated polymers (CPs) is beneficial to boosting the NRR process and at the same time suppressing the competing hydrogen evolution reaction. Of particular interest, it is found that a semicrystalline CP catalyst, SC-PBDT-TT, exhibits a high Faradaic efficiency of up to 60.5% with a maximum NH_3 production rate of 16.8 μg h^{-1} mg^{-1} in a neutral-buffered seawater electrolyte. Molecular dynamics and COMSOL Multiphysics simulations reveal the origin of the observed high NRR performance arising from the presence of desirable crystal regions to resist the penetration of H_2O molecules, leading to the formation of a "quasi-gas–solid" interface inside the catalyst for a favorable direct-contact between the catalyst and N_2 molecules. Furthermore, high-throughput computations, based on density functional theory, reveal the actual real active site for N_2 adsorption and reduction in SC-PBDT-TT. This work provides a new framework for optimizing NRR performance of metal-free catalysts by controlling their crystallinities.

1. Introduction

Electrochemical nitrogen reduction reaction (NRR) under mild conditions has recently become a very hot research topic, as it provides an alternative clean strategy to replace the energy-intensive and massive CO_2-producing Haber–Bosch process for green ammonia (NH_3) production.[1–4] As one of the most abundant natural resources on the earth, seawater accounts for above 96.5% of the planet's total water amount and can in principle be used as a cost-effective natural electrolyte for water-splitting reactions.[5–7] In order to conserve scarce freshwater to which salts have to be added to make it an electrolyte, the direct use of seawater electrolyte during electrochemical NRR processes would represent an interesting environmental benign approach. It would require, however the development of corresponding electrocatalysts that maintain

F. Lai, T. Liu
The Key Laboratory of Synthetic and Biological Colloids
Ministry of Education
School of Chemical and Materials Engineering
International Joint Research Laboratory for Nano Energy Composites
Jiangnan University
Wuxi 214122, P. R. China
E-mail: txliu@jiangnan.edu.cn

F. Lai, J. Hofkens
Department of Chemistry
KU Leuven
Celestijnenlaan 200F, Leuven 3001, Belgium
E-mail: johan.hofkens@kuleuven.be

J. Huang, L. Dai
Australian Carbon Materials Centre (A-CMC)
School of Chemical Engineering, UNSW Sydney
Sydney, NSW 2052, Australia
E-mail: l.dai@unsw.edu.au

J. Huang
School of Chemical Engineering
Zhengzhou University
Zhengzhou 450001, P. R. China
E-mail: huangjiajia@zzu.edu.cn

X. Liao
Institute of Advanced Scientific Research (iASR) & Key Laboratory of Functional Small Molecules for Ministry of Education
Jiangxi Normal University
99 Ziyang Avenue, Nanchang 330022, P. R. China
E-mail: xfliao@jxnu.edu.cn

W. Zong, F. Gan, Y. Fang, Y.-E. Miao
State Key Laboratory for Modification of Chemical Fibers and Polymer Materials
College of Materials Science and Engineering
Innovation Center for Textile Science and Technology
Donghua University
Shanghai 201620, P. R. China

L. Ge
School of Chemistry
University of Bristol
Cantock's Close
Bristol BS8 1TS, UK

J. Hofkens
Department of Molecular Spectroscopy
Max Planck Institute for Polymer Research
Ackermannweg 10, 55128 Mainz, Germany

The ORCID identification number(s) for the author(s) of this article can be found under https://doi.org/10.1002/adma.202201853.

DOI: 10.1002/adma.202201853

structural stability under such conditions. Unlike the so far explored metal-containing electrocatalysts, including noble metals (for example, Au, Pd, Rh, Pt–Ir alloy, etc.)[8–12] and non-noble metals/compounds (for example, Bi, $NiCo_2O_4$, MoS_2, ReS_2, etc.),[13–16] metal-free catalysts avoid intrinsic drawbacks associated with those metal catalysts, such as high cost, toxicity, limited abundance of rare metals (particularly, noble metals) in nature, and negative environmental effect. Recently reported metal-free electrocatalysts for NRR consist mostly of carbon materials, such as heteroatoms-doped carbons (N or B),[17–20] boron carbides,[21] and carbon nitrides.[22] The catalytic mechanism of carbon-based metal-free electrocatalysts has been widely attributed to the doping-induced charge-transfer, leading to inhomogeneous charge distribution.[23,24] Owing to the versatility and ill-defined structures associated with carbon materials, however, the structure-property relationship for carbon catalysts and its influence on the NRR performance has not been well understood.

As a new class of emerging metal-free electrocatalysts, donor–acceptor (D–A) based conjugated polymers (CPs) are of particular interest because their semiconductor properties (e.g., the band gaps, band positions, and p/n characteristic) can be easily tuned through a selection of appropriate donor and acceptor units.[25–27] They not only provide an ideal platform to investigate the structure-property relationships, but also promote the D–A-based CPs as metal alternatives for electrocatalysis. In this regard, the presence of a D–A heterojunction can regulate the charging mobility in D–A-based CPs to create an inhomogeneous charge distribution between donor and acceptor units.[28] This partial charge delocalization occurs in every individual D–A segment of the CP and can act as active sites for nitrogen adsorption and reduction. However, the poor periodicity and abundant functional groups in many D–A-based CPs make the experimental identification of the active sites for the NRR process a difficult task, if not impossible, whereas it is much easier for most inorganic materials due to their crystalline periodic structures. High-throughput first-principle calculations have been reported as a highly-efficient strategy to reveal the active sites in D–A-based CPs.[29,30]

The active sites in D–A-based CPs are likely to be occupied by H_2O molecules to activate the adverse hydrogen evolution reaction (HER) and compete for the NRR process, due to the preferential adsorption of hydrogen atoms over nitrogen atoms in water.[31] Several efficient strategies have been put forward recently to suppress the HER: 1) Ling et al. covered the NRR electrocatalyst with a superhydrophobic metal–organic framework layer to significantly suppress the HER process and boost the NRR Faradaic efficiency by several percentages;[32] 2) Yan et al. used acidic potassium sulfate electrolyte to stabilize the key nitrogen-reduction intermediates and regulate proton transfer, leading to a Faradaic efficiency as high as 66% for NRR;[13] 3) Yan et al. used single iron atoms on nitrogen-doped carbon support as the electrocatalyst to positively shift the onset potential with a dramatically enhanced Faradaic efficiency of 56.55%.[33] On the other hand, the hydrophobicity of a polymer is closely related to its degree of crystallinity (DC), as reported in previous reports.[34–36] However, its implication to NRR electrocatalysis has yet to be recognized. The well-designed crystalline surface of CPs can withstand the penetration of H_2O molecules to a certain degree and partially restrict their contact with the tightly wrapped active sites in the inner crystalline region of the CPs. Thus, a perfect crystalline surface may suppress the HER process significantly, while a suitable NRR electrocatalyst still needs the participation of protons (H_2O or H_2) in the reaction to realize the reduction of N_2. Therefore, the design of CPs-based electrocatalysts with the right fraction of crystallinity is not only "terra incognita" but also an important issue to boost green ammonia production.

In this study, we designed the semicrystalline CP SC-PBDT-TT with an 8.50% degree of crystalline determined by wide-angle X-ray diffraction (WAXD). The SC-PBDT-TT catalyst was used as a metal-free electrocatalyst for the NRR process and exhibited an excellent Faradaic efficiency of 60.5% with a high NH_3 production rate of 16.8 $\mu g\ h^{-1}\ mg^{-1}$ at –0.7 V in the neutral-buffered seawater electrolyte. This outstanding NRR performance is attributable to the presence of right crystal regions in the SC-PBDT-TT catalyst to generate a "quasi-gas–solid" interface between the N_2 gas and the catalyst, as evidenced by molecular dynamics and COMSOL Multiphysics simulations (vide infra). Furthermore, high-throughput computations based on the density functional theory (DFT) were conducted to precisely determine the active site for N_2 adsorption and reduction in the SC-PBDT-TT catalyst with the rate-determining step ($*NH_2 \rightarrow *$) of a 2.18 eV energy barrier.

2. Results and Discussion

Three different electron acceptors (A) and two types of electron donors (D) are displayed in **Figure 1**a,b. Series 1 represents different electron-acceptor variations, including B68, BDD, and TT, while Series 2 shows two kinds of electron-donor units of BDT and 3TDC. Based on these units, three D–A alternating CPs, namely PB68-3TDC, PBDB-T, and PBDT-TT (Figures S1–S3, Supporting Information), were designed by complexing one electron-acceptor monomer and one electron-donor monomer from series 1 and 2, respectively, at a predetermined molar ratio. Due to the dipolar and inductive effects,[37] the electron in every D–A segment is partially delocalized from the D to the A units, leading to a higher electron density in the A unit compared to the D unit. This inhomogeneous electron distribution creates numerous sites of high electron density to act as active sites for electrochemical NRR (vide supra).

Figure 1c shows the band structures (HOMO and LUMO band positions) established by the DFT calculations. As can be seen, PBDT-TT displays HOMO positions close to the reduction potential of N_2 in different environments, which are –4.92 and –5.16 eV in the gas phase and water, respectively, indicating its potential as a highly active NRR electrocatalyst. Furthermore, the three D–A polymers (PB68-3TDC, PBDB-T, and PBDT-TT) show different electron densities on the HOMO and LUMO levels (Figure 1d and Figure S4, Supporting Information). In particular, the electron in PBDT-TT distributes along the backbone through its conjugated segments, demonstrating its good conductivity for electron transfer during the electrocatalytic NRR process, as we shall see later.

Because of the above discussion, TT (compound 1) and BDT (compound 2) were used as monomers to synthesize PBDT-TT

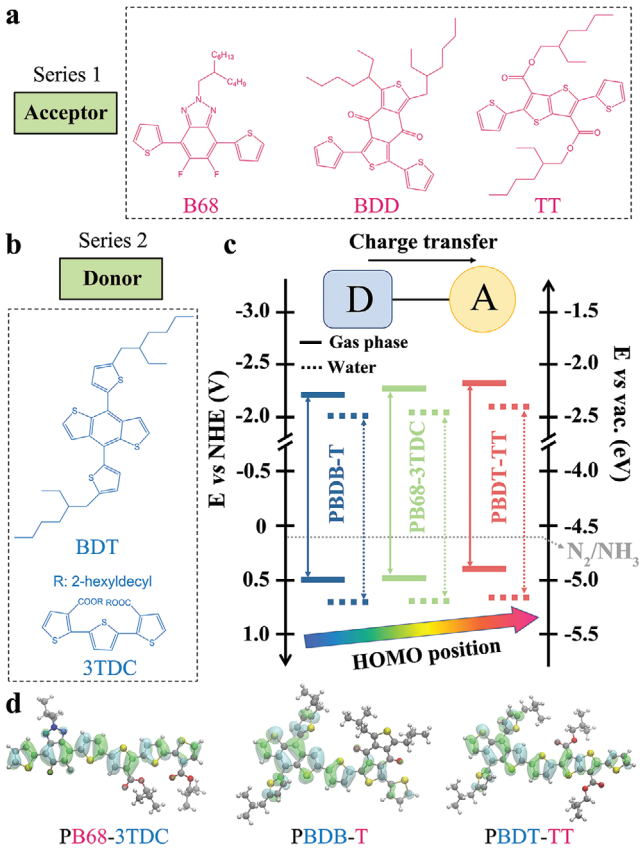

Figure 1. Two series of polymeric units for possible donor–acceptor polymers: a) acceptor and b) donor. c) Band structure diagram for various donor–acceptor polymers in different environments (gas phase and water). d) HOMO levels for the segments of PB68-3TDC, PBDB-T, and PBDT-TT.

(**Figure 2**a) with details in the Supporting Information. In order to suppress the adverse HER by the hydrophobic surface discussed above, we deliberately controlled the DC for PBDT-TT by tuning the crystallization conditions, leading to the generation of three samples: low-crystalline PBDT-TT (LC-PBDT-TT), semicrystalline PBDT-TT (SC-PBDT-TT), and high-crystalline PBDT-TT (C-PBDT-TT). The degree of crystallization was characterized by high-resolution transmission electron microscopy (HRTEM) and wide-angle X-ray diffraction (WAXD) measurements. The LC-PBDT-TT displays an amorphous structure without obvious crystalline zones as seen in the corresponding HRTEM images (Figure 2b and Figure S5, Supporting Information). The corresponding HRTEM images for the SC-PBDT-TT sample (Figure 2c and Figure S6, Supporting Information) show small crystalline grains (particle size: ≈3.5 nm) appeared among the amorphous regions with rich crystal boundaries. For the HC-PBDT-TT sample, it exhibits abundant crystalline grains in its HRTEM image (Figure 2d), demonstrating its high DC. To estimate the crystallinity quantitatively, Figure 2e–g shows the 2D WAXD patterns for LC-PBDT-TT, SC-PBDT-TT, and HC-PBDT-TT, respectively, which reveals the order of intermolecular packing increased from LC-PBDT-TT, through SC-PBDT-TT, to HC-PBDT-TT, in good consistency with the HRTEM images. For more detailed analyses, 1D integrated WAXD intensity profiles of these samples are shown in Figure 2h–j, where radical 2θ scans were carried out. Curve-fitting deconvolution of the intensity profiles along the equator was performed using Peak-fit Software to separate various phase contributions. The DCs in the different PBDT-TT samples were estimated by calculating the ratio of the integral area of crystalline scattering to the total integral areas of crystalline and amorphous scatterings. The DCs for LC-PBDT-TT, SC-PBDT-TT, and HC-PBDT-TT were found to be 3.46%, 8.50%, and 15.01%, respectively. From the N_2 physisorption experiments at –196 °C (Figure S7, Supporting Information), the specific surface area values of LC-PBDT-TT, SC-PBDT-TT, and HC-PBDT-TT are calculated to be in a narrow range between 3 and 10 $m^2\ g^{-1}$, which suggests that the modulated DCs of PBDT-TT have a negative effect on its specific surface area. The near-edge X-ray absorption fine structure (NEXAFS) analysis (Figure S8, Supporting Information) provides additional structural details of the synthesized SC-PBDT-TT, which matches well with its molecular structure (Scheme S1, Supporting Information). More structural information on various PBDT-TT samples was provided by Fourier transform infrared (FTIR) spectroscopy (Figure S9, Supporting Information), Raman analyses (Figure S10, Supporting Information), and ^1H nuclear magnetic resonance (NMR) spectroscopy (Figure S11, Supporting Information) with corresponding discussion in the Supporting Information, which demonstrate that the molecular structures of the synthesized PBDT-TT remain unchanged for LC-PBDT-TT, SC-PBDT-TT, and HC-PBDT-TT. Furthermore, three PBDT-TT samples of different DCs with co-existing crystalline and amorphous phases (Figure 2k–m) will be used as three models to reveal the relationship between the crystalline property and electrochemical NRR performance for the D–A-based CP catalysts.

In order to conserve scarce freshwater and extra salt for electrolytes, natural seawater was selected as the electrolyte for the following NRR tests. To hinder the formation of insoluble precipitates, such as magnesium hydroxide ($Mg(OH)_2$),[38] the pH of the collected seawater (pH = 8.0) from the nearby coastal site (**Figure 3**a and Figure S12, Supporting Information) was precisely controlled and preferably maintained within the neutral range by using the NaH_2PO_4/Na_2HPO_4 acid/base conjugate pair as a buffer. Based on the calibration curves for NH_3 detection in the neutral-buffered seawater electrolyte by using the indophenol blue method (Figure S13, Supporting Information), the ammonia content in the neutral-buffered seawater electrolyte during the NRR process was estimated from the result of ultraviolet (UV) intensity. Prior to its use, a series of blank experiments were carried out to confirm the purity of neutral-buffered seawater electrolyte (Figure S14, Supporting Information), under N_2/Ar gases (Figure S15, Supporting Information), and $^{15}N_2$ gas (Figure S16, Supporting Information) to demonstrate there is no NH_3 contamination in these systems. In order to exclude the possible NH_3 contaminations from SC-PBDT-TT catalyst and carbon paper substrate, we further conducted another two blank experiments (Figure S17, Supporting Information).

By employing PBDT-TT of different DCs as the cathodic catalysts, potentiostatic NRR tests were conducted by bubbling N_2 gas continuously at ambient temperature and pressure

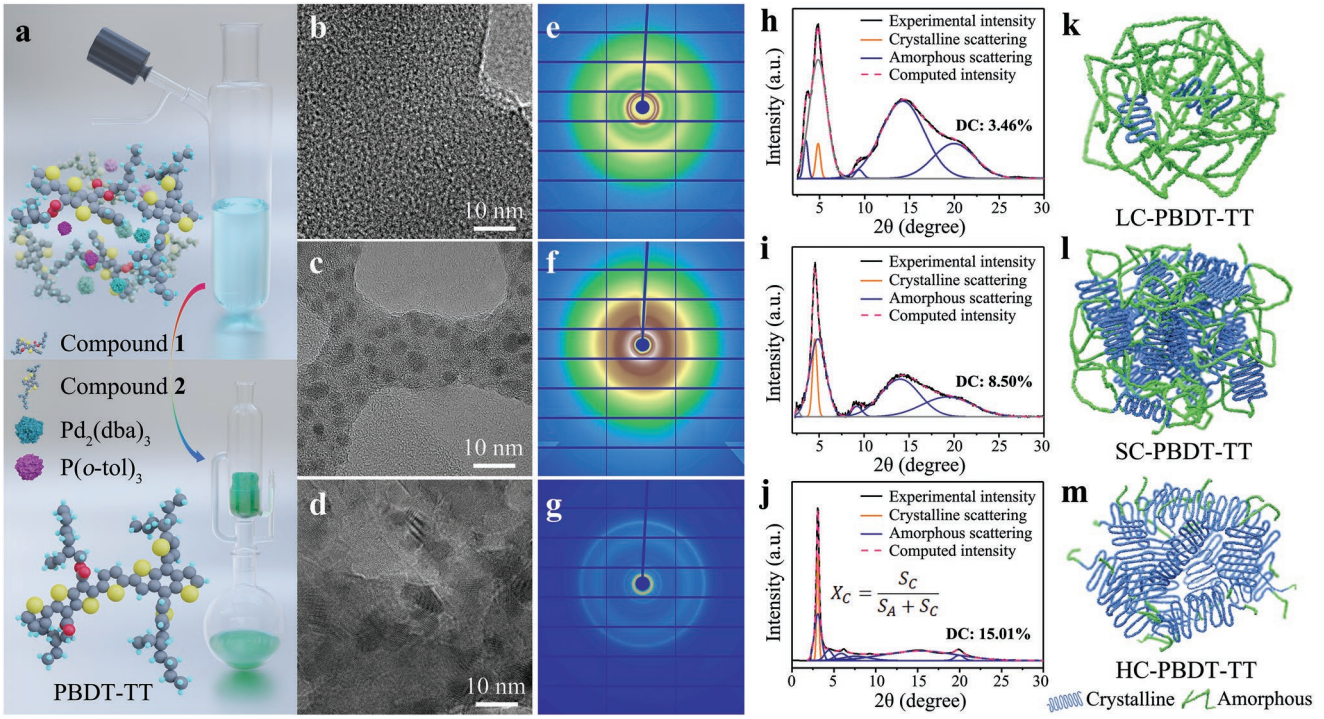

Figure 2. a) Synthesis of polymer PBDT-TT by using compounds 1 and 2 as monomers. b–d) HRTEM images of LC-PBDT-TT (b), SC-PBDT-TT (c), and HC-PBDT-TT (d). e–g) WAXD patterns of LC-PBDT-TT (e), SC-PBDT-TT (f), and HC-PBDT-TT (g). h–j) 1D integrated WAXD intensity profile and the corresponding peak separation analysis to estimate the crystallinity in LC-PBDT-TT (h), SC-PBDT-TT (i), and HC-PBDT-TT (j). k–m) Illustration for the microstructures of three PBDT-TT samples with different DCs: k) LC-PBDT-TT, l) SC-PBDT-TT, and m) HC-PBDT-TT.

(Figure S18a, Supporting Information). As shown in Figure 3b, the highest NH_3 yield rate was calculated to be 16.8 μg h^{-1} mg^{-1} for the SC-PBDT-TT catalyst with the maximum Faradaic efficiency of 60.5% when the potential reaches –0.7 V. Faradaic efficiency of SC-PBDT-TT reduces with reducing potential from –0.7 V, reflecting the enhanced competition of HER process as the proton reduction becomes easier.[38–40] Meanwhile, the coverage on the surface of the SC-PBDT-TT catalyst with H_2 would confine the penetration of N_2 gas into the inner space of the SC-PBDT-TT catalyst, leading to the limited NH_3 yield rate during the NRR process. When the potential locates at a more positive region than the inflection point, the NH_3 yield rate decreases dramatically due to the limited amount of electrons available to reduce N_2 into NH_3, as confirmed by the linear-sweep voltammetry curve (Figure S18b, Supporting Information). The decreased Faradaic efficiency indicates the applied electrons are much easier to combine with H_2O molecule and reduce H_2O into H_2 when the potential is more negative than –0.7 V. Furthermore, it was noted that the NRR activity for SC-PBDT-TT is much higher than the one of in the LC-PBDT-TT catalyst (NH_3 yield rate: 5.4 μg h^{-1} mg^{-1}; Faradaic efficiency: 16.1%) and of the HC-PBDT-TT catalyst (NH_3 yield rate: 7.7 μg h^{-1} mg^{-1}; Faradaic efficiency: 31.6%), as well as many other metal-free electrocatalysts (Figure 3c and Table S3, Supporting Information).[17,19,21,22,41–48] Additionally, the electrochemical surface areas (ECSAs) of LC-PBDT-TT, SC-PBDT-TT, and HC-PBDT-TT catalysts were determined by the double layer capacitances (C_{dl}) in their corresponding cyclic voltammetric (CV) curves (Figure S19a–c, Supporting Information), which are 7.2, 6.2, and 5.4 mF cm^{-2} (Figure S19d, Supporting Information), respectively.[49,50] From the perspective of ESCAs, the SC-PBDT-TT catalyst also shows the highest NH_3 production rate (for additional discussion, see Supporting Information). Electrochemical impedance spectroscopy (EIS) analysis of SC-PBDT-TT was also conducted and shown in Figure S20, Supporting Information, indicating a low charge transfer resistance between the catalyst and electrolyte interface.[51] These results demonstrate the positive effects of the semicrystalline structure on both NH_3 yield rate and Faradaic efficiency, which will be further illustrated by the following molecular dynamics (MD) and COMSOL Multiphysics simulations. Impressively, no N_2H_4 by-product was detected in the neutral-buffered seawater electrolyte (Figure S21, Supporting Information) by the Watt and Chrisp method,[9] demonstrating the high selectivity of SC-PBDT-TT catalyst for NH_3 generation.

Catalytic stability is another key feature to evaluate the potential practical use of electrocatalysts. During long-term electrocatalytic tests (50 cycles) at an applied potential of –0.7 V, the SC-PBDT-TT catalyst displayed a small decay in both NH_3 yield rate and Faradaic efficiency (Figure 3d). Specifically, the NH_3 yield rate remains at a level of 87.5% of its initial value and shows well-maintained structural features (Figures S22 and S23, Supporting Information), implying the excellent stability of the SC-PBDT-TT catalyst in the NRR process. Although the possible contaminations from the SC-PBDT-TT catalyst itself have been ruled out (Figure S17, Supporting Information), and isotopic labeling experiment was also employed in 0.1 M Na_2SO_4 electrolyte to trace the nitrogen origin in the NH_3

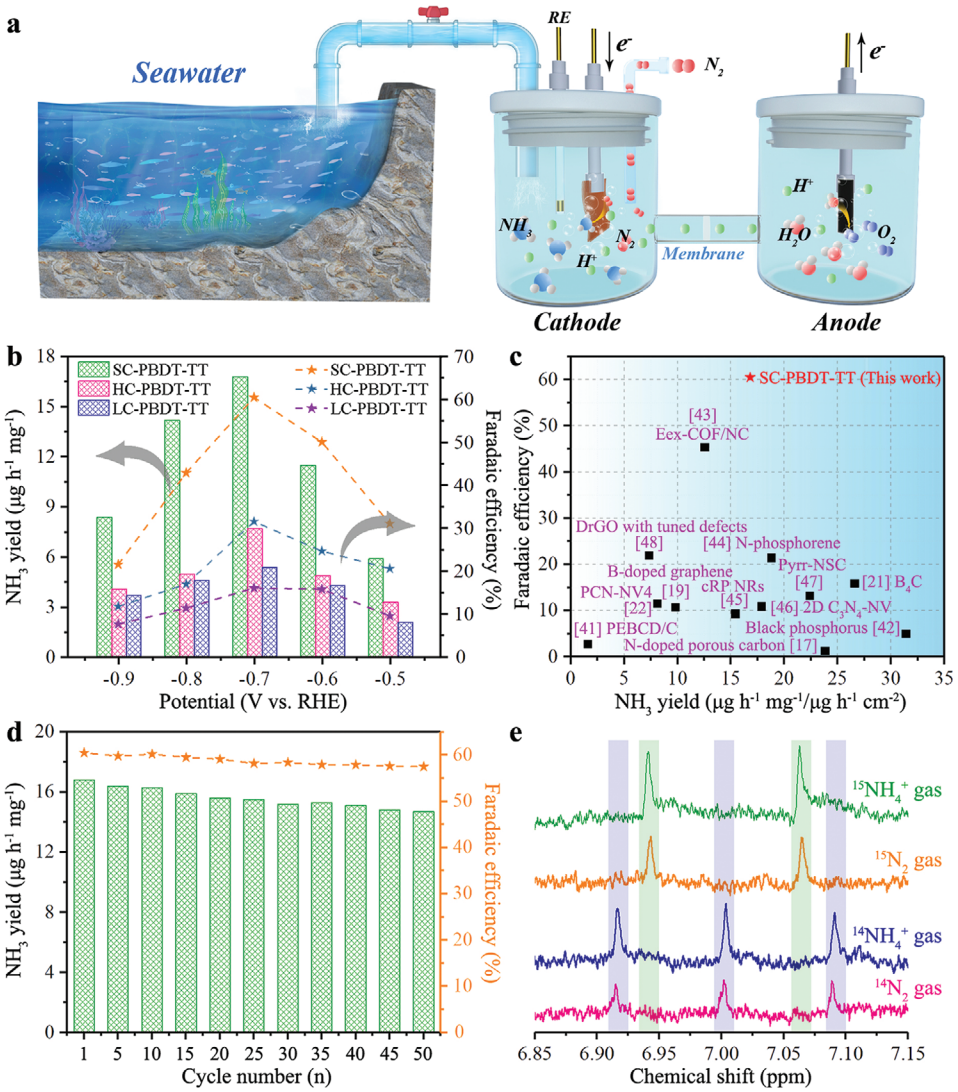

Figure 3. Electrochemical NRR performance in neutral-buffered seawater electrolyte. a) Schematic illustration for the neutral-buffered seawater electrolysis. Here, RE means reference electrode. b) NH_3 yield rate and Faradaic efficiency of SC-PBDT-TT, HC-PBDT-TT, and LC-PBDT-TT at different potentials. c) Comparison of NRR properties reported recently referring to metal-free electrocatalysts. d) Recycling test (50 cycles) of SC-PBDT-TT at an applied potential of –0.7 V (vs RHE). e) ^1H NMR analysis of SC-PBDT-TT fed by $^{14}N_2$ and $^{15}N_2$ gases after electrochemical NRR process in 0.1 M Na_2SO_4 electrolyte.

production (Figure 3e). Here, the ^1H NMR spectra of commercial $(^{14}NH_4)_2SO_4$ and $(^{15}NH_4)_2SO_4$ samples were collected as two standard models, which show a ^{14}N triplet (I = 1) and a ^{15}N double (I = 1/2) between 6.85 to 7.15 ppm, respectively. The NMR spectra of electrochemical systems fed by $^{14}N_2$ and $^{15}N_2$ gases well correspond to the two standard models. More importantly, there is no ^{14}N triplet in the NMR spectrum for the system fed by $^{15}N_2$, demonstrating the detected NH_3 production fully originates from the nitrogen gas instead of the SC-PBDT-TT catalyst itself.

To understand the impact of semicrystalline characteristic of SC-PBDT-TT on the diffusion of nitrogen and water, MD simulations were conducted. For simplicity, the SC-PBDT-TT model was constructed by connecting the crystalline region (Figure S24, Supporting Information) between two amorphous regions as displayed in **Figure 4**a, where the height of the channel was fixed as 1.5 nm. The simulation box was filled with a gas-liquid mixture of 14 118 water molecules and 2340 nitrogen molecules. The initial structure for the simulation was set up by filling the gas-liquid mixture in the two amorphous regions at 0 ps (Figure 4a), where the direction from left to right in the as-constructed model was defined as the Z-direction. As the diffusion proceeds from 0 to 10 000 ps, we found abundant N_2 molecules can penetrate into the channels (crystalline region) gradually while the H_2O molecules are confined outside (Figure 4a & Figure S25, Supporting Information). When the diffusion time is between 9 and 10 ns, the average numbers of N_2 and H_2O molecules along the Z-direction of the SC-PBDT-TT model were counted in Figure 4b. Statistically speaking, the occupancy of the H_2O molecule in the crystalline region of the SC-PBDT-TT model (from 10.2 to 27.7 nm along the Z-direction) decreases dramatically, while the occupancy of the N_2 molecule

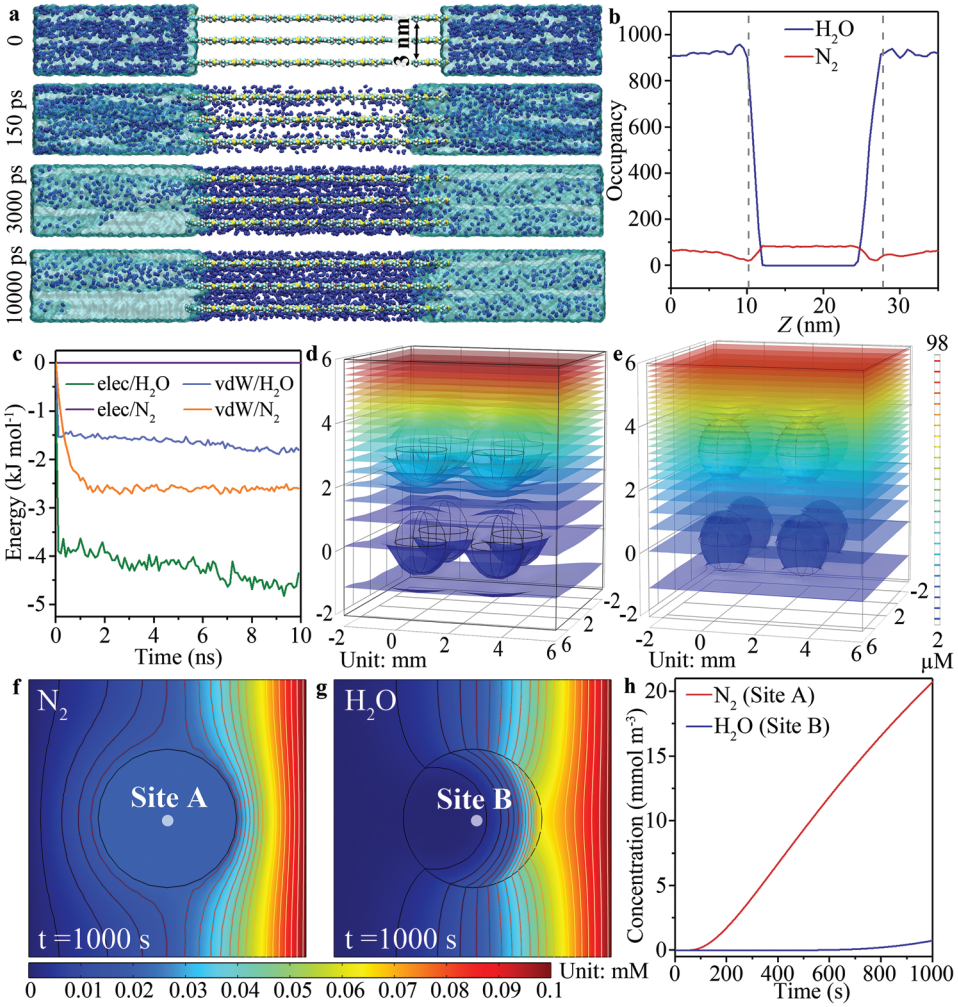

Figure 4. MD and COMSOL Multiphysics simulations for the N_2 and H_2O diffusions. a) Snapshots of the N_2 and H_2O distributions in the crystalline region of the SC-PBDT-TT model from 0 to 10 000 ps. The cyan, yellow, red, white, and blue balls represent C, S, O, H, and N atoms, respectively. b) The N_2 and H_2O occupancies along the *Z*-direction (from left to right in the crystalline region of the SC-PBDT-TT model) between 9 and 10 ns. c) Electrostatic and vdW interactions of N_2 and H_2O with SC-PBDT-TT. d,e) Distributions of N_2 concentration (d) and H_2O concentration (e) in the 3D simulation domain of SC-PBDT-TT at 5000 s. f,g) Distributions of N_2 concentration (f) and H_2O concentration (g) around the crystalline region of SC-PBDT-TT at 1000 s. h) The changes of N_2 and H_2O concentrations in the center of the crystalline region of SC-PBDT-TT within 1000 s.

increases slightly. Although the dynamic diameter of the H_2O molecule (≈4.0 Å) is similar to that of the N_2 molecule (≈3.6 Å), H_2O molecules in the natural-buffered seawater electrolyte are easily clustered with each other due to the existence of abundant sodium ions and strong hydrogen bonds, resulting in a large size for the water phase and a mismatch with the height of the channel (1.5 nm) in the crystalline region of SC-PBDT-TT. However, the inert N_2 molecules with a small dynamic diameter (≈3.6 Å) are not easy to be bunched together, which leads to their fast diffusion inside the crystalline region compared to the H_2O. On the other hand, we also investigated the diffusion of N_2 and H_2O molecules into the amorphous region of SC-PBDT-TT. As shown in Figure S26, Supporting Information, both N_2 and H_2O molecules can penetrate into the amorphous region and occupy the free space of SC-PBDT-TT gradually from 0 to 2000 ps, which points to poor selectivity of the amorphous region in SC-PBDT-TT. The average number of N_2 and H_2O molecules along the *Z*-direction of the amorphous region of SC-PBDT-TT (Figure S27a, Supporting Information) also provides quantitative evidence of its poor selectivity, where the occupancy of H_2O molecule drops slowly and even reaches a higher level than that of N_2 molecule (from 1.6 to 8.2 nm along the *Z*-direction). In stark contrast, the occupancy of H_2O molecule in the crystalline region is close to zero (Figure S27b, Supporting Information, similar as in Figure 4b), which firmly demonstrates that only the crystalline region in SC-PBDT-TT can act hydrophobic and aerophilic behaviors. Therefore, the as-confirmed existence of hydrophobic and aerophilic behaviors of the crystalline region in the SC-PBDT-TT model is beneficial for the generation of a "quasi-gas–solid" interface in the interior space of the catalyst. As a result, abundant active sites in the crystalline region can come in contact with the N_2 gas directly, leading to the suppressed HER and accelerated NRR processes. In addition, further analyses of the van der Waals (vdW) and electrostatic interactions

of the two molecules (N_2 and H_2O) with a selected region of SC-PBDT-TT (Figure 4c) indicate that the SC-PBDT-TT exhibits stronger vdW attractions towards the N_2 molecules compared to H_2O molecules. These results imply that the stronger nitrogen adsorption ability for the SC-PBDT-TT and enhanced NRR performance originates from its semicrystalline structure.

To further elucidate the structural superiority of SC-PBDT-TT with a "quasi-gas–solid" interface in the interior space of the catalyst, COMSOL Multiphysics simulations were performed by constructing a 3D simulation domain ($8 \times 8 \times 8$ mm^3, Figure S28, Supporting Information), in which both the N_2 and H_2O diffuse from top to bottom (with eight spheres presenting the crystalline regions in SC-PBDT-TT). The COMSOL Multiphysics simulations were conducted by using transport of diluted species modules with more details in the Supporting Information. When the diffusion time reaches 5000 s, the distributions of N_2 and H_2O concentrations in the 3D simulation domain of the SC-PBDT-TT are displayed in Figure 4d,e. In particular, the N_2 gas has already penetrated into the crystalline region, while the H_2O molecules almost gathered outside the spheres, in the amorphous region. It also confirms the hydrophobic and aerophilic behavior of the crystalline region in SC-PBDT-TT. In order to monitor the diffusion processes better, we also recorded the changes (from 0 to 1000 s) of N_2 and H_2O concentrations in the center of the sphere in site A (Figure 4f) and site B (Figure 4g), respectively. As plotted in Figure 4h, the N_2 concentration increases rapidly after 70 s. However, only a slight H_2O penetration occurs at site B, which indicates the diffusion of H_2O in the crystalline region is much more difficult than that of N_2. All these results demonstrate that the hydrophobic crystalline region in the SC-PBDT-TT is beneficial for the generation of a "quasi-gas–solid" interface in the interior space of the catalyst, resulting in a suppressed HER process and abundant unoccupied active sites for the NRR process (especially in the crystalline region of SC-PBDT-TT).

Apart from the diffusion of N_2 and H_2O molecules inside the SC-PBDT-TT, the exact active site in the PBDT-TT chain is further unveiled by high-throughput computational DFT calculation. Unlike the simple atomic structures in many inorganic materials with perfect periodicity, the CP-based catalyst consists of different functional groups (see **Figure 5**a), which makes it difficult to determine the real active site in PBDT-TT for nitrogen adsorption and reduction. Here, the PBDT-TT segment was split into 70 fragments and marked as 1 to 70. Thereafter, one N_2 molecule would scan and touch these 70 sites to calculate the corresponding binding energy (BE) from left to right automatically. To be noted, the BE indicates the smallest amount of energy required to remove the adsorbed N_2 on the PBDT-TT ($*N_2$) catalyst into individual PBDT-TT (*) and N_2. As a result, the BE values on the interfaces between different groups in PBDT-TT and N_2 are plotted in Figure 5b and Table S4, Supporting Information. As the first nitrogen adsorption is regarded as the key step during the overall NRR process, there are three preferred active sites (site 2, site 6,

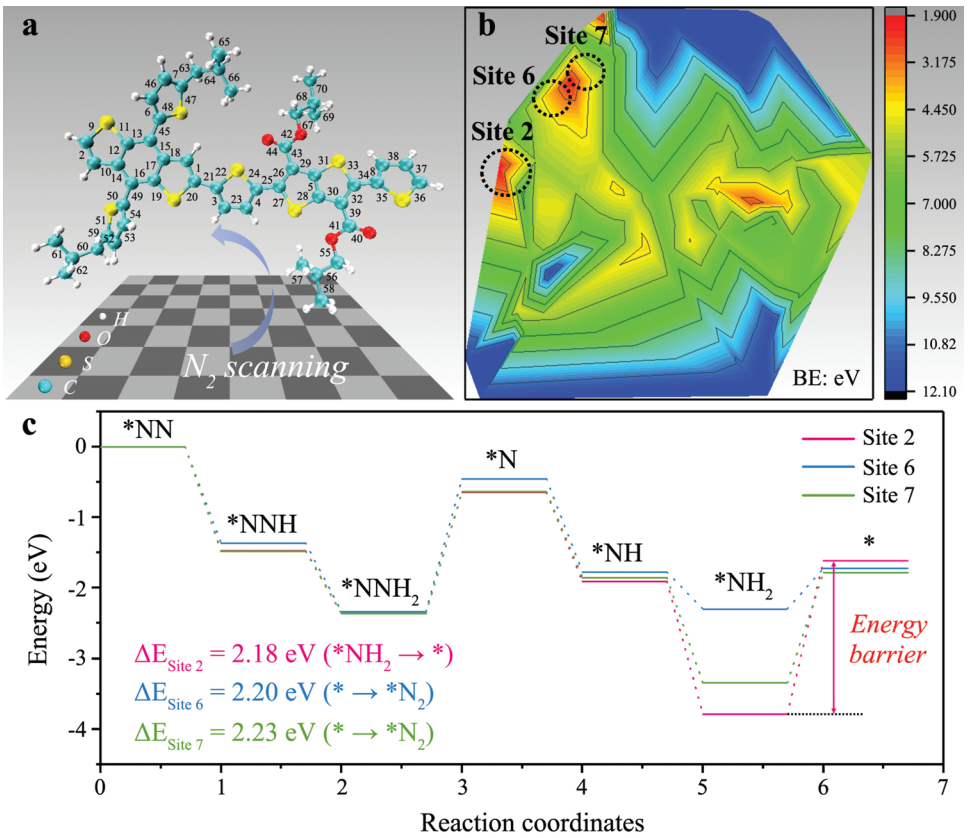

Figure 5. a) The optimized model of PBDT-TT with marked 70 sites for N_2 scanning. b) The calculated BE with the N_2 molecule residing on different sites of the PBDT-TT model. c) The energy diagrams for NRR on different sites (Site 1, Site 2, and Site 6) of PBDT-TT.

and site 7) identified for the subsequent N_2 reduction after high-throughput computational screening. These sites show BE values of 1.99, 2.20, and 2.23 eV, respectively, the lowest among the 70 sites, indicating the main active sites for N_2 adsorption are located at thiophene rings rather than on the alkane side-chains. The optimized structures of N_2 adsorbed PBDT-TT on different sites are also provided in Figure S29, Supporting Information. The average bond lengths between carbon and adsorbed N atoms on site 2, site 6, and site 7 are measured as 1.512, 1.487, and 1.502 Å, respectively, indicating their chemically stable structures for the subsequent nitrogen reduction steps. More precisely, the associative distal pathway is suggested (Figure S30, Supporting Information) and studied on site 2, site 6, and site 7. As the corresponding energy diagrams shown in Figure 5c (more details of energy data can be found in Table S5, Supporting Information), the N_2 adsorption is coincidentally the rate-determining step for site 6 and site 7 with energy barriers of 2.20 and 2.23 eV, respectively. For site 2, the last step during the NRR process ($*NH_2 \rightarrow *$) is regarded as the rate-determining step with an energy barrier of 2.18 eV. These results indicate that site 2 has the lowest energy barrier and is the most likely site for N_2 adsorption and reduction in the PBDT-TT chain from a DFT perspective.

3. Conclusions

We have revealed a new strategy to optimize the nitrogen reduction reaction (NRR) performance of polymeric metal-free catalysts by regulating their degree of crystalline. First, a donor–acceptor-based conjugated polymer (CP) of PBDT-TT was chosen and synthesized as an NRR catalyst based on its appropriate HOMO position with respect to the reduction potential of N_2. From the NRR performance in neutral-buffered seawater electrolyte, it was found that the semicrystalline PBDT-TT (SC-PBDT-TT) catalyst displayed a boosted Faradaic efficiency (60.5% at –0.7 V) and a maximum NH_3 yield rate (16.8 μg h^{-1} mg^{-1}). As revealed by molecular dynamics and COMSOL Multiphysics simulations, the observed outstanding NRR performance is attributable to the presence of the appropriate crystal regions in the SC-PBDT-TT to generate the desirable "quasi-gas–solid" interface (between N_2 and catalyst) by limiting the penetration of H_2O molecules to suppress the competitive hydrogen evolution reaction. Finally, the exact active site for NRR in the SC-PBDT-TT catalyst was precisely revealed by analyzing 70 fragments through high-throughput computations based on DFT calculation to find the lowest energy barrier for the rate-determining step ($*NH_2 \rightarrow *$) to be 2.18 eV. This work clearly shows the positive effect of crystal structure in donor–acceptor-based CPs to boost their NRR performance, providing important guidance for the design of next-generation metal-free catalysts for the NRR process and beyond.

Supporting Information

Supporting Information is available from the Wiley Online Library or from the author.

Acknowledgements

The authors are grateful for the financial support from the National Natural Science Foundation of China (52161135302, 21674019, 51873198, 51973032, and 21905043), the Research Foundation Flanders (G0F2322N), the Shanghai Scientific and Technological Innovation Project (18JC1410600), the Program of the Shanghai Academic Research Leader (17XD1400100), the Thousand Talents Plan of Jiangxi Province (jxsq2019101051), and Jiangxi Provincial Natural Science Foundation (20212ACB203005). J.H. gratefully acknowledges the financial support from the Flemish Government through the Moonshot cSBO project P2C (HBC. 2019.0108) and through long-term structural funding (Methusalem CASAS2, Meth/15/04) and from the Interne Fondsen KU Leuven through project C3/20/067. L.D. is grateful for partial support from ARC (DP 190103881 and FL 190100126). The NEXAFS experiments were carried out at beamline 4B9B of the Beijing Synchrotron Radiation Facility (BSRF). Great thanks to Dr. C. Liu for the help with measurement. Theoretical work was carried out at the LvLiang Cloud Computing Center of China, and the calculations were performed on a TianHe-2 system.

Conflict of Interest

The authors declare no conflict of interest.

Data Availability Statement

The data that support the findings of this study are available from the corresponding author upon reasonable request.

Keywords

conjugated polymers, nitrogen fixation, seawater electrolytes, semicrystalline materials

Received: February 26, 2022
Revised: June 20, 2022
Published online: July 31, 2022

[1] C. Guo, J. Ran, A. Vasileff, S.-Z. Qiao, *Energy Environ. Sci.* **2018**, *11*, 45.
[2] G.-F. Chen, S. Ren, L. Zhang, H. Cheng, Y. Luo, K. Zhu, L.-X. Ding, H. Wang, *Small Methods* **2018**, *2*, 1800337.
[3] X. R. Chen, Y. T. Guo, X. C. Du, Y. S. Zeng, J. W. Chu, C. H. Gong, J. W. Huang, C. Fan, X. F. Wang, J. Xiong, *Adv. Energy Mater.* **2020**, *10*, 1903172.
[4] N. Legnert, H. T. Dong, J. B. Harland, A. P. Hunt, C. J. White, *Nat. Rev. Chem.* **2018**, *2*, 278.
[5] A. J. Esswein, Y. Surendranath, S. Y. Reece, D. G. Nocera, *Energy Environ. Sci.* **2011**, *4*, 499.
[6] F. Dionigi, T. Reier, Z. Pawolek, M. Gliech, P. Strasser, *ChemSusChem* **2016**, *9*, 962.
[7] L. Y. Zhang, Z. Y. Wang, J. S. Qiu, *Adv. Mater.* **2022**, *34*, 2109321.
[8] Y. Yao, S. Q. Zhu, H. J. Wang, H. Li, M. H. Shao, *J. Am. Chem. Soc.* **2018**, *140*, 1496.
[9] D. Bao, Q. Zhang, F.-L. Meng, H.-X. Zhong, M.-M. Shi, Y. Zhang, J.-M. Yan, Q. Jiang, X.-B. Zhang, *Adv. Mater.* **2016**, *29*, 1604799.
[10] J. Wang, L. Yu, L. Hu, G. Chen, H. Xin, X. Feng, *Nat. Commun.* **2018**, *9*, 1795.
[11] H.-M. Liu, S.-H. Han, Y. Zhao, Y.-Y. Zhu, X.-L. Tian, J.-H. Zeng, J.-X. Jiang, B. Y. Xia, Y. Chen, *J. Mater. Chem. A* **2018**, *6*, 3211.

[12] Y.-J. Mao, L. Wei, X.-S. Zhao, Y.-S. Wei, J.-W. Li, T. Sheng, F.-C. Zhu, N. Tian, Z.-Y. Zhou, S.-G. Sun, *Chem. Commun.* **2019**, *55*, 9335.
[13] Y.-C. Hao, Y. Guo, L.-W. Chen, M. Shu, X.-Y. Wang, T.-A. Bu, W.-Y. Gao, N. Zhang, X. Su, X. Feng, J.-W. Zhou, B. Wang, C.-W. Hu, A.-X. Yin, R. Si, Y.-W. Zhang, C.-H. Yan, *Nat. Catal.* **2019**, *2*, 448.
[14] F. L. Lai, J. R. Feng, X. B. Ye, W. Zong, G. J. He, C. Yang, W. Wang, Y.-E. Miao, B. C. Pan, W. S. Yan, T. X. Liu, I. P. Parkin, *J. Mater. Chem. A* **2020**, *8*, 1652.
[15] J. Li, S. Chen, F. J. Quan, G. M. Zhan, F. L. Jia, Z. H. Ai, L. Z. Zhang, *Chem* **2020**, *6*, 885.
[16] F. L. Lai, N. Chen, X. B. Ye, G. J. He, W. Zong, K. B. Holt, B. C. Pan, I. P. Parkin, T. X. Liu, *Adv. Funct. Mater.* **2020**, *30*, 1907376.
[17] Y. M. Liu, Y. Su, X. Quan, X. F. Fan, S. Chen, H. T. Yu, H. M. Zhao, Y. B. Zhang, J. J. Zhao, *ACS Catal.* **2018**, *8*, 1186.
[18] S. Mukherjee, D. A. Cullen, S. Karakalos, K. Liu, H. Zhang, S. Zhao, H. Xu, K. L. More, G. Wang, G. Wu, *Nano Energy* **2018**, *48*, 217.
[19] X. M. Yu, P. Han, Z. X. Wei, L. S. Huang, Z. X. Gu, S. J. Peng, J. M. Ma, G. F. Zheng, *Joule* **2018**, *2*, 1610.
[20] Y. Song, D. Johnson, R. Peng, D. K. Hensley, P. V. Bonnesen, L. Liang, J. Huang, F. Yang, F. Zhang, R. Qiao, A. P. Baddorf, T. J. Tschaplinski, N. L. Engle, M. C. Hatzell, Z. Wu, D. A. Cullen, H. M. MeyerIII, B. G. Sumpter, A. J. Rondinone, *Sci. Adv.* **2018**, *4*, e1700336.
[21] W. Qiu, X.-Y. Xie, J. Qiu, W.-H. Fang, R. Liang, X. Ren, X. Ji, G. Cui, A. M. Asiri, G. Cui, B. Tang, X. Sun, *Nat. Commun.* **2018**, *9*, 3485.
[22] C. D. Lv, Y. M. Qian, C. S. Yan, Y. Ding, Y. Y. Liu, G. Chen, G. H. Yu, *Angew. Chem., Int. Ed.* **2018**, *57*, 10246; *Angew. Chem.* **2018**, *130*, 10403.
[23] K. Gong, F. Du, Z. Xia, M. Durstock, L. Dai, *Science* **2009**, *323*, 760.
[24] C. Hu, R. Paul, Q. Dai, L. Dai, *Chem. Soc. Rev.* **2021**, *50*, 11785.
[25] H. Xu, J. Gao, D. Jiang, *Nat. Chem.* **2015**, *7*, 905.
[26] N. Chaoui, M. Trunk, R. Dawson, J. Schmidt, A. Thomas, *Chem. Soc. Rev.* **2017**, *46*, 3302.
[27] Z.-A. Lan, G. G. Zhang, X. Chen, Y. F. Zhang, K. A. I. Zhang, X. C. Wang, *Angew. Chem., Int. Ed.* **2019**, *58*, 10236; *Angew. Chem.* **2019**, *131*, 10342.
[28] C. Deibel, T. Strobel, V. Dyakonov, *Adv. Mater.* **2010**, *22*, 4097.
[29] M. Zhong, K. Tran, Y. M. Min, C. H. Wang, Z. Y. Wang, C.-T. Dinh, P. D. Luna, Z. Q. Yu, A. S. Rasouli, P. Brodersen, S. Sun, O. Voznyy, C.-S. Tan, M. Askerka, F. L. Che, M. Liu, A. Seifitokaldani, Y. J. Pang, S.-C. Lo, A. Ip, Z. Ulissi, E. H. Sargent, *Nature* **2020**, *581*, 178.
[30] L. Kahle, A. Marcolongo, N. Marzari, *Energy Environ. Sci.* **2020**, *13*, 928.
[31] C. J. M. van der Ham, M. T. M. Koper, D. G. H. Hetterscheid, *Chem. Soc. Rev.* **2014**, *43*, 5183.
[32] H. K. Lee, C. S. L. Koh, Y. H. Lee, C. Liu, I. Y. Phang, X. Han, C.-K. Tsung, X. Y. Ling, *Sci. Adv.* **2018**, *4*, 3208.
[33] M. Wang, S. Liu, T. Qian, J. Liu, J. Zhou, H. Ji, J. Xiong, J. Zhong, C. Yan, *Nat. Commun.* **2019**, *10*, 341.
[34] M. A. Naeem, P. F. Lv, H. M. Zhou, T. Naveed, Q. F. Wei, *Polymers* **2018**, *10*, 712.
[35] Y. Cho, H. R. Lee, A. Jeong, J. Lee, S. M. Lee, S. H. Joo, S. K. Kwak, J. H. Oh, C. Yang, *ACS Appl. Mater. Interfaces* **2019**, *11*, 40347.
[36] M. Khodaie, A. Saeidi, H. A. Khonakdar, J. Seyfi, I. Hejazi, S. M. Davachi, H. Bahmanpour, *Prog. Org. Coat.* **2020**, *140*, 105534.
[37] H. Bronstein, J. M. Frost, A. Hadipour, Y. Kim, C. B. Nielsen, R. S. Ashraf, B. P. Rand, S. Watkins, I. McCulloch, *Chem. Mater.* **2013**, *25*, 277.
[38] M. F. Wang, S. S. Liu, T. Qian, J. Liu, J. Q. Zhou, H. Q. Ji, J. Xiong, J. Zhong, C. L. Yan, *Nat. Commun.* **2019**, *10*, 341.
[39] F. L. Lai, W. Zong, G. J. He, Y. Xu, H. W. Huang, B. Weng, D. W. Rao, J. A. Martens, J. Hofkens, I. P. Parkin, T. X. Liu, *Angew. Chem., Int. Ed.* **2020**, *59*, 13320; *Angew. Chem.* **2020**, *132*, 13422.
[40] Y. Y. Ma, T. Yang, H. Y. Zou, W. J. Zang, Z. K. Kou, L. Mao, Y. P. Feng, L. Shen, S. J. Pennycook, L. L. Duan, X. Li, J. Wang, *Adv. Mater.* **2020**, *32*, 2002177.
[41] G.-F. Chen, X. R. Cao, S. Q. Wu, X. Y. Zeng, L.-X. Ding, M. Zhu, H. H. Wang, *J. Am. Chem. Soc.* **2017**, *139*, 9771.
[42] L. L. Zhang, L.-X. Ding, G.-F. Chen, X. F. Yang, H. H. Wang, *Angew. Chem., Int. Ed.* **2019**, *58*, 2612; *Angew. Chem.* **2019**, *131*, 2638.
[43] S. Liu, M. Wang, T. Qian, H. Ji, J. Liu, C. Yan, *Nat. Commun.* **2019**, *10*, 3898.
[44] G. R. Xu, H. Li, A. S. R. Bati, M. Bat-Erdene, M. J. Nine, D. Losic, Y. Chen, J. G. Shapter, M. Batmunkh, T. Y. Ma, *J. Mater. Chem. A* **2020**, *8*, 15875.
[45] Q. Liu, X. Zhang, J. H. Wang, Y. L. Zhang, S. Bian, Z. Q. Cheng, N. Kang, H. Huang, S. Gu, Y. Wang, D. N. Liu, P. K. Chu, X.-F. Yu, *Angew. Chem., Int. Ed.* **2020**, *59*, 14383; *Angew. Chem.* **2020**, *132*, 14489.
[46] Z. M. Zhao, Y. Long, S. Luo, Y. T. Luo, M. Chen, J. T. Ma, *J. Energy Chem.* **2021**, *60*, 546.
[47] W. Q. Zhang, K. K. Mao, J. X. Low, H. J. Liu, Y. N. Bo, J. Ma, Q. X. Liu, Y. W. Jiang, J. Z. Yang, Y. Pan, Z. M. Qi, R. Long, L. Song, Y. J. Xiong, *Nano Res.* **2021**, *14*, 3234.
[48] M. L. Zhang, C. Choi, R. P. Huo, G. H. Gu, S. Hong, C. Yan, S. Y. Xu, A. W. Robertson, J. S. Qiu, Y. Jung, Z. Y. Sun, *Nano Energy* **2020**, *68*, 104323.
[49] A. A. Kashale, A. V. Ghule, I.-W. P. Chen, *ChemCatChem* **2021**, *13*, 1165.
[50] Y.-M. Lai, A. A. Kashale, M.-H. Liu, W.-S. Liao, C.-Y. Chang, W.-Y. Chen, Y.-H. Chan, I.-W. P. Chen, *ACS Appl. Nano Mater.* **2022**, *5*, 2163.
[51] A. A. Kashale, C.-H. Yi, K.-Y. Cheng, J.-S. Guo, Y.-H. Pan, I.-W. P. Chen, *ACS Appl. Energy Mater.* **2020**, *3*, 10831.